International Journal of Non–Linear Mechanics 163 (2024) 104765

Contents lists available at ScienceDirect

International Journal of Non-Linear Mechanics

journal homepage: www.elsevier.com/locate/nlm

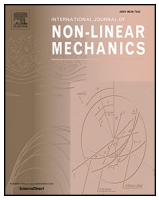

Letter to the Editor

Multi-state dynamics and model similarity of a vibro-impact nonlinear system

ARTICLE INFO

Keywords
Vibro-impact
High-dimensional system
Chaotic and multi-state dynamics
Piece-wise and continuous VI model

ABSTRACT

Vibro-impact (VI) can generate strong nonlinearities into mechanical systems. Despite extensive research, the chaotic and multi-state dynamics of VI systems are not fully understood, and modeling high-dimensional systems with multiple VI oscillators remains a challenge. This study analyzes a typical 3 degrees of freedom (DOF) VI system to elucidate its chaotic dynamic behavior. We propose a criterion for replacing the piece-wise VI model with a continuous one to streamline the modeling, speed up calculations, and facilitate system analysis. We investigate the similarity of the two models in terms of predicting system response and chaotic dynamics. Numerical and experimental findings show that with increased nonlinearity, a 3DOF VI system degenerates to a 2DOF system, due to the collisional and non-collisional states between the two oscillators. This results in discontinuous multi-state transmission curves and simultaneous resonance suppression. Moreover, by incorporating higher-order nonlinear functions, the continuous model's responses align more closely with the piece-wise model, albeit at a higher computational cost. While both models exhibit similar chaotic dynamics, the piece-wise model exhibits a higher degree of chaos. Reducing damping and the collision gap is recommended to maintain high prediction accuracy across a range of nonlinearities. These findings enhance the understanding of the multi-state and chaotic dynamics of VI motion and pave the way for the accurate and efficient modeling of strongly nonlinear, high-dimensional metamaterial systems.

1. Introduction

The intentional introduction of nonlinearities into mechanical systems is known to offer numerous benefits [1–4]. Understanding the dynamics of typical nonlinear systems is crucial for their design and modeling, as well as for harnessing specific nonlinear properties to mitigate low-frequency, broadband vibrations. Notably, the Nonlinear Energy Sink (NES) [5–8] and the more recent Nonlinear Elastic Metamaterials [2,9,10] (NEM, a system consisting of periodic nonlinear unit cells) have been developed with the aim of reducing vibrations. However, a significant challenge lies in achieving the required level of strong nonlinearity at a small or moderate excitation amplitude typically encountered in mechanical systems. In this regard, vibro-impact (VI) systems, including VI-based NESs, have garnered significant attention due to the exotic dynamics they can offer. The subtle use of VI motion has been proven to generate strong nonlinearity at a moderate amplitude, a concept that has been effectively exploited in the field of NEM [11,12]. Yet, the task of computing the responses of high-dimensional systems, which comprise many VI oscillators, such as the typical configuration used in metamaterials, is challenging.

In addition, the chaotic and multi-state dynamics of VI systems are not entirely comprehended. Consequently, this paper concentrates on exploring the dynamics and modeling of VI systems. We review advancements in the field with a particular focus on the generation and modeling of VI effects, using NES and NEM systems as illustrative examples.

Nonlinear Energy Sinks (NESs) contain oscillators that are connected to a primary system to enable rapid and passive energy transfer and dissipation. Various NES configurations have been proposed, including those that rely on cubic nonlinearity [13–15], rotary NESs [16–19], track NESs [20–22] and VI NESs [23–26]. A VI NES is particularly noteworthy for its non-smooth nonlinearity, which is not only effective across different excitation types and magnitudes but also practically feasible to implement [7]. Recently, in a two-degree-of-freedom primary system with two VI NESs, numerical investigations focusing on target energy transfers (TET) have demonstrated their energy absorption efficiency under shock excitation [27]. In a multi-DOF primary system with multiple VI NESs, the performance for seismic mitigation has been compared through both numerical simulations and experimental studies to identify the most effective configurations under various conditions [28–30]. The nonlinear dynamics that facilitate this exceptional energy absorption have been the subject of extensive research. For instance, in a single DOF primary system with a VI NES, the system dynamics have been analyzed through Hamiltonian frequency-energy plots (FEPs), revealing complex transitions between periodic and quasi-periodic motions [31]. In a 2DOF primary system with a VI NES, mathematical investigations into the FEPs have uncovered bifurcations and fractal characteristics of periodic orbits at nonlinear normal modes [32]. While these studies have provided valuable insights into the performance and transient dynamics of VI NESs, there remains a gap in the analysis of steady-state dynamics, particularly regarding the chaotic behaviors induced by VI motion.

The research on NESs has predominantly focused on simplistic configurations with one or a few NESs. In contrast, NEM consists of arrays of nonlinear oscillators, theoretically extending to infinite numbers. Strong nonlinearities within NEM, often a result of VI motion, have been shown to yield extraordinary properties, such as ultra-low and ultra-wide-band vibration suppression [33], bridging of bandgap couplings [34],

https://doi.org/10.1016/j.ijnonlinmec.2024.104765
Received 6 February 2024; Received in revised form 2 April 2024; Accepted 23 May 2024
Available online 24 May 2024

adaptive bandgap broadening [12], and nonreciprocal wave propagation [35]. Although VI motion is advantageous for the design and empirical validation of NEMs, the computational challenges associated with collisional states, non-collisional states, and velocity discontinuities at critical points are significant [11,12]. To address these challenges, an "equivalent" continuous nonlinear function has been employed in previous NEM studies to model the non-smooth or VI functions [11,12]. However, the efficacy and accuracy of this approach have not undergone rigorous validation.

Although VI motion has been successfully utilized to induce strong nonlinearity at a moderate amplitude, understanding its complex chaotic and multi-state dynamics during steady-state excitation remains an open question. For example, a system with n degrees of freedom may behave akin to a system with fewer DOF when in collisional or non-collisional states, giving rise to complex phenomena on the transmission curves. The onset of chaotic dynamics could lead to abrupt changes in the time domain response, which are not yet fully understood. The use of VI oscillators in experimental NEMs highlights the challenge of computing and simulating high-dimensional VI systems using piece-wise VI models. In response, a continuous model has been suggested as an alternative to expedite calculations, but the criteria for such a transition have not been thoroughly explored. It is essential to establish the "similarity" between the two models to ensure the reliability of the continuous model and the true representation of the physics.

This paper analyzes the multi-state chaotic dynamics in the steady-state response of a 3DOF VI system and investigates the response and chaotic dynamics of the system and assess the similarity between the piece-wise and continuous VI models. More specifically, Section 2 introduces the VI system and formulates a continuous VI model using a series of "equivalent" continuous functions to represent the piece-wise functions. It also details the numerical and analytical methodologies for determining the steady-state response. Section 3 presents the discontinuous multi-state characteristics with increasing nonlinearity and examines the nonlinear and chaotic dynamics using the piece-wise and continuous VI models. Section 4 explores the system response and chaotic dynamics of the system and examine the similarity between both models using different continuous functions. Section 5 discusses an experimental validation of the multi-state and chaotic dynamics observed in the piece-wise VI model. This research underpins future precise and efficient analytical and numerical modeling for high-dimensional, strongly nonlinear NEM systems.

2. Model and methods

We examine the dynamics of a typical 3DOF vibro-impact (VI) system as depicted in Fig. 1(a), alongside the dynamics' similarity with the continuous VI model portrayed in Fig. 1(b). This model epitomizes

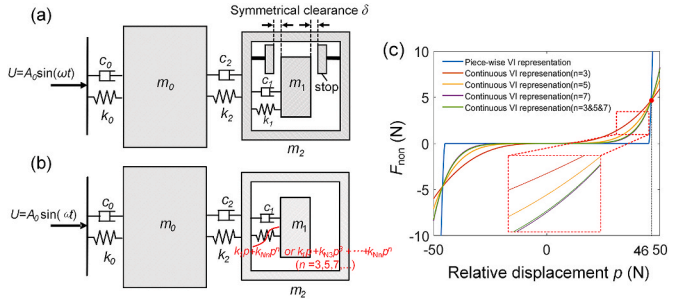

Fig. 1. Models. (a) Schematic of the piece-wise VI model, (b) Schematic of the continuous VI model, (c) Interactive force F_{non} between m_1 and stops in piece-wise and continuous VI models. Continuous VI models ($n = 3$, 5, 7 and 3&5&7) mean that continuous function $k_{\text{N3}}p^3$, $k_{\text{N5}}p^5$, $k_{\text{N7}}p^7$ and $k_{\text{N3}}p^3+k_{\text{N5}}p^5+k_{\text{N7}}p^7$ are used to replace the symmetrical piece-wise function.

nonlinear energy sinks and typical nonlinear local resonators found in metamaterials, as referenced in Ref. [12]. The model comprises three oscillators, labeled m_0, m_1 and m_2, each interconnected by distinct springs and dampers. The displacements of m_0, m_1 and m_2 are x, y and z, respectively, while the relative displacement is denoted as $p = y-z$. Oscillator m_0 is connected to the external displacement input $U(t)$ via linear stiffness k_0 and damping coefficient c_0; similarly, m_2 is linked to m_0 through a linear stiffness k_2 and damper c_2. Apart from a linear spring k_1 and damper c_1 situated between m_1 and m_2, two rigid boundaries affixed to m_2 limit the relative displacement $p = y-z$ between m_1 and m_2. In the equilibrium state, the clearances, or gap δ between m_1 and each boundary are symmetrical. Consequently, collisions between m_1 and m_2 occur when $|p| \geq \delta$. The equations of motion for the entire model write:

$$\begin{cases} m_0\ddot{x} = k_2(z-x) + k_0(U-x) + c_2(\dot{z}-\dot{x}) + c_0(\dot{U}-\dot{x}) \\ m_1(\ddot{p}+\ddot{z}) = -k_1 p - F_{\text{non}} - c_1\dot{p} \\ m_2\ddot{z} = -k_2(z-x) + k_1 p + F_{\text{non}} - c_2(\dot{z}-\dot{x}) + c_1\dot{p} \end{cases} \tag{1}$$

in which F_{non} denotes the interactive force between m_1 and each boundary, as described in Fig. 1(c). In practice, the collision between m_1 and m_2 is dominated by the contact force and deformation. Therefore, we adopt the typical Hertz contact model between a sphere and plane to describe the nonlinear force, i.e.,

$$F_{\text{non}} = \begin{cases} k_{\text{contact}}(p-\delta)^{1.5} & (p \geq \delta) \\ 0 & (|p| < \delta) \\ -k_{\text{contact}}(-p-\delta)^{1.5} & (p \leq -\delta) \end{cases} \tag{2}$$

where $k_{\text{contact}} = \frac{4}{3}ER^{\frac{1}{2}}$ denotes the contact stiffness, $\frac{1}{E} = \frac{1-\nu_1{}^2}{E_1} + \frac{1-\nu_2{}^2}{E_2}$, in which E_1 and E_2 are the elastic moduli, and ν_1, ν_2 the Poisson's ratios associated with each body. In the experiments (to be detailed later), nonlinearity arises from the contact between a sphere and a cylindrical surface, which can be precisely modeled by the Hertzian contact theory as detailed in Ref. [36]. This model has demonstrated its reliability in describing the nonlinear dynamics between the contacting bodies. Notably, the same Hertzian model has also been extensively applied in studies of granular materials [37–40]. In the present case, m_1 is a sphere, colliding with the plane surface of m_2 to meet the requirement of the typical Hertz contact model. Taken from a recent experimental configuration [12], the materials of sphere m_1 and the two stops are steel ($E_1 =$ 206 Gpa, $\nu_1 = 0.27$) and aluminum alloy ($E_2 = 67$ Gpa, $\nu_2 = 0.3$), respectively. Natural frequencies of the individual oscillators are denoted by $\omega_i = \sqrt{k_i/m_i} = 2\pi f_i$, $i = 0, 1, 2$. Parameters are: $m_0 = 5.8$ g, $m_1 =$ 2.1 g, $m_2 = 2$ g; $f_0 = 322$ Hz, $f_1 = 100$ Hz, and $f_2 = 390.6$ Hz. The radius of m_1 is determined as $R = 4.4$ mm based on the steel sphere mass of 2.1 g. The damping coefficient $c_i = 0.01k_i$, $i = 0, 1, 2$. A range of values for δ were tested, and ultimately $\delta = 45$ μm was determined. This value not only meets the manufacturing precision requirements but also generates the desired strong nonlinearity under a moderate excitation amplitude.

We establish a continuous VI model as shown in Fig. 1(b) in which the symmetrical piecewise function is approximated by a continuous function:

$$F_{\text{non}} \approx k_{\text{Nn}}p^n \;\; or \;\; F_{\text{non}} \approx k_{\text{N3}}p^3 + \ldots + k_{\text{Nn}}p^n \;\; (n = 3, 5, 7, \ldots) \tag{3}$$

Only odd-order terms are considered due to structural symmetry; k_{Ni} denotes the i-order nonlinear stiffness coefficient. To achieve closer alignment between the continuous and piecewise VI models, we determine k_{Ni} by fitting the piece-wise curve, as shown in Fig. 1(c). Given that the small dynamic load between m_1 and m_2 induces only minor contact deformation at the boundary [12], we take the contact force when $p =$ 46 μm (*i.e.,* the contact deformation is 1 μm) to obtain the coefficients k_{Ni}. That is: $k_{\text{Nn}}p^n$ or $k_{\text{N3}}p^3 + \ldots + k_{\text{Nn}}p^n = k_{\text{contact}}(p\text{-}\delta)^{1.5}$. Practically, the value of p may be modified to suit the specific system configuration.

The response of the continuous VI model can be analytically solved with the first-order harmonic balance method. Let

$$\mathbf{X} = \mathbf{A}\cos(\omega t) + \mathbf{B}\sin(\omega t) \tag{4}$$

in which $\mathbf{X} = [X, P, Z]^{\mathrm{T}}$; X, P and Z denote the amplitude of x, p and z, respectively; $\omega = 2\pi f$. $U(t) = A_0\sin(\omega t)$. Substituting Eq. (4) into (1) and balancing the coefficients of $\sin(\omega t)$ and $\cos(\omega t)$, one can obtain the solution for different continuous VI models with different nonlinear terms. For example, when $n = 5$, one has

$$\begin{cases} (\mathbf{K} - \omega^2\mathbf{M})\mathbf{A} + \omega\mathbf{C}\mathbf{B} + \frac{5}{8}k_{\mathrm{N5}}\left(\mathbf{A}^2 + \mathbf{B}^2\right)^2\mathbf{A} = [c_0\omega A_0, 0, 0]^T \\ (\mathbf{K} - \omega^2\mathbf{M})\mathbf{B} - \omega\mathbf{C}\mathbf{A} + \frac{5}{8}k_{\mathrm{N5}}\left(\mathbf{A}^2 + \mathbf{B}^2\right)^2\mathbf{B} = [k_0A_0, 0, 0]^T \end{cases} \tag{5}$$

By specifying the input amplitude A_0 and input frequency ω, the eigenvector of $\mathbf{A}$ and $\mathbf{B}$ can be obtained. Consequently, the normalized steady response is derived as $[X, P, Z]^{\mathrm{T}}/A_0 = (\mathbf{A}\mathbf{A}^{\mathrm{T}} + \mathbf{B}\mathbf{B}^{\mathrm{T}})^{0.5}/A_0$.

For both piece-wise and continuous VI models, we also calculate the system response using a numerical integration approach. In the simulations, the input displacement $U(t)$ is a monoharmonic function. An integration time of 30 s is selected, which is sufficiently long to achieve steady state, as depicted in Fig. 2. We consider two types of response amplitudes: (1) taking the maximum amplitude during the last 5 s of the time-domain signal; (2) calculating the frequency spectrum of the signal and taking the component amplitude of the input frequency f, as shown in Fig. 2(b). The results obtained from the two methods are labeled as "Response I and Response II" hereafter, respectively. For linear systems (with $k_{\mathrm{N}n} = 0$), Response I is the same as Response II. For nonlinear systems, Response I embraces the total energy containing multiple frequency components under a given input frequency, whereas Response II represents only one frequency component. Hence, as shown in Fig. 2(c), the generalized Response II may be significantly lower than Response I. Moreover, the generalized responses indicate that the VI oscillator is capable of suppressing the three resonances, a phenomenon that will be explored in subsequent sections.

3. Dynamics of the two VI models

3.1. Dynamics of the piece-wise VI model

Fig. 3 shows Responses I and II for the piece-wise VI model under four excitation amplitude levels, $A_0 = 1$, 5, 10, 50 μm, which are representatives of weak, moderate, and strong nonlinear states, respectively. The shaded regions in Fig. 3 highlight the frequency ranges where the linear and nonlinear responses diverge.

For weak nonlinearity at $A_0 = 1$ μm, Responses I, II and the linear response all show identical resonance peaks at 95, 266 and 500 Hz. As A_0 increases, the amplitudes of Responses I and II jump up or down around the resonance frequencies, exhibiting discontinuous multi-state features.

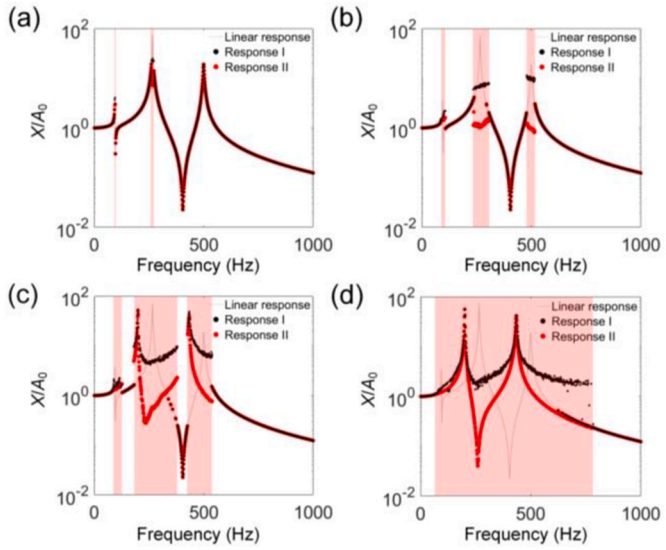

Fig. 3. Normalized response of m_0 in the piece-wise VI model with increasing input amplitude A_0. Herein, we take four typical cases to show the variation process of Response I & II. (a) Case-1: weak nonlinearity ($A_0 = 1$ μm), (b) Case-2: moderate nonlinearity ($A_0 = 5$ μm), (c) Case-3: moderate nonlinearity ($A_0 = 10$ μm), (d) Case-4: strong nonlinearity ($A_0 = 50$ μm). The shading region represents that the collision between m_1 and m_2 happens.

Concurrently, the initial three resonances vanish, supplanted by alternate resonant frequencies. A typical case for $A_0 = 5$ μm is used to elucidate this discontinuous phenomenon, as shown in Fig. 4. The normalized relative displacement p in Fig. 4(a) can reveal the collisional or non-collisional states between m_1 and m_2.

When $|p| \le \delta = 45$ μm, implying no collision, the response is linear. When $|p| > \delta$, the collision occurs, but p barely increases and remains saturated because the high contact stiffness limits the observable deformation. Moreover, as highlighted in the shaded areas, the dynamics undergo significant changes upon collision. The frequency response curve exhibits jumping between linear non-collisional and nonlinear collisional states. With an increase in A_0, collisional regions begin to supplant non-collisional ones. Under strong nonlinearity at $A_0 = 50$ μm, the initial three resonances are completely replaced by two new resonances at 201 and 435 Hz, with Responses I and II appearing nearly continuous. The two frequencies remain constant at larger amplitudes, signifying them as terminal resonances. Consequently, the 3DOF system behaves as a 2DOF system in such case, because when the collision occurs (p almost stays saturated), m_1 and m_2 are "bound"

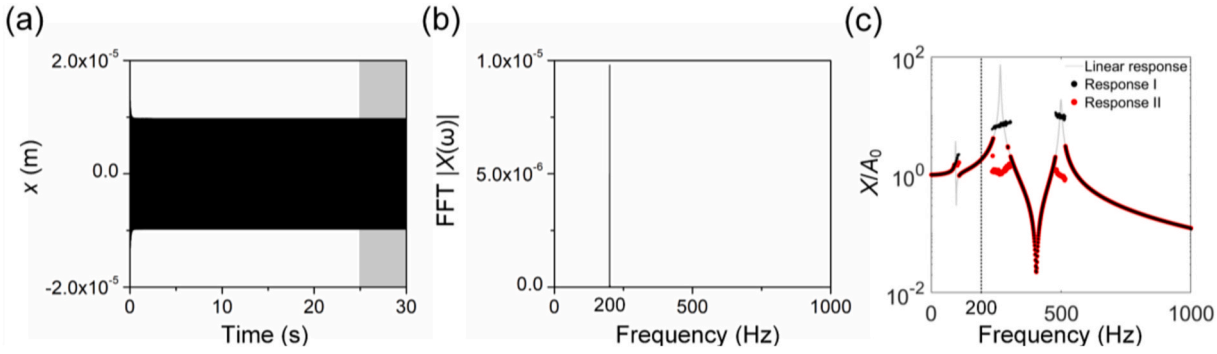

Fig. 2. Response of m_0 in the VI system when $A_0 = 5$ μm. (a) Time domain when $f = 200$ Hz. Black area corresponds to the last 5 s response, (b) Frequency spectra of the last 5 s of (a) (black area). The frequency spectra were obtained by the fast Fourier transform (FFT), (c) Normalized linear response and Responses I & II. Responses I & II were nonlinear response extracted by two different date processing methods. Responses I& II in the dash line ($f = 200$ Hz) were extracted from (a) and (b).

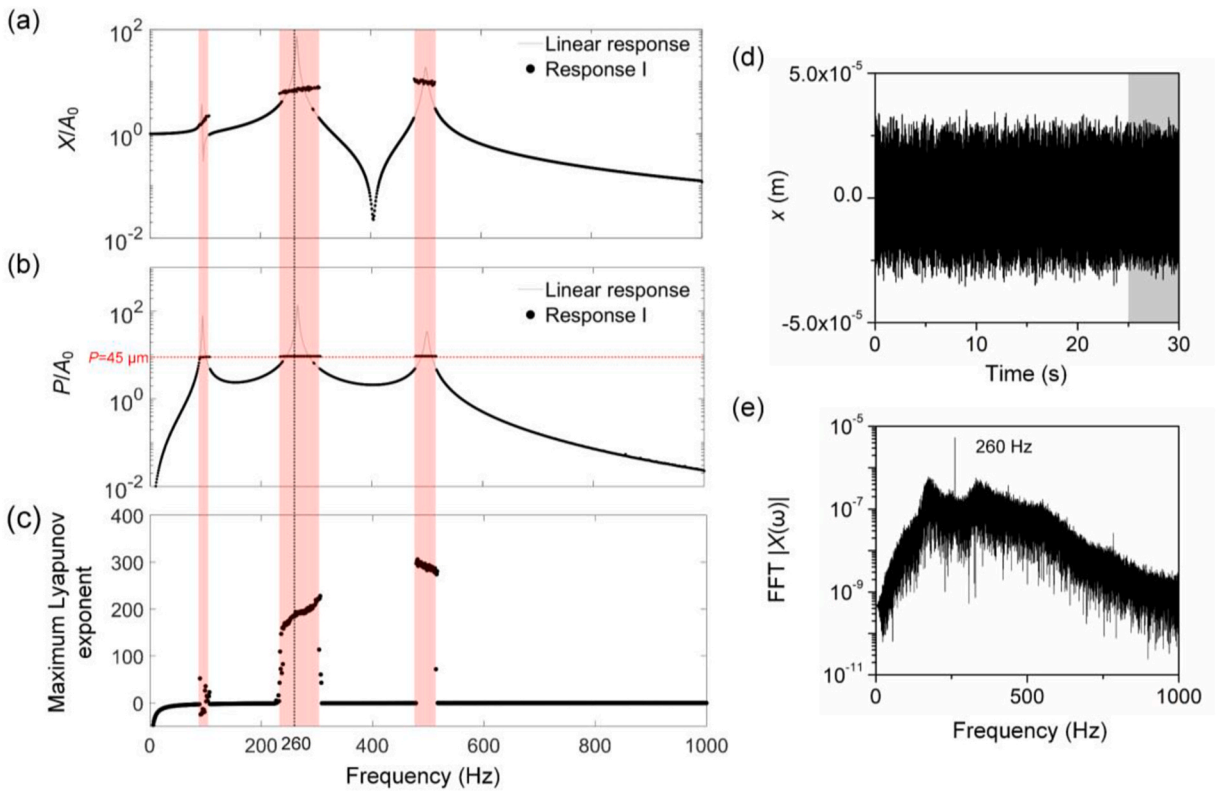

Fig. 4. Response in the piece-wise VI model when $A_0 = 5$ μm. (a) Normalized linear response and Responses I of m_0, (b) Normalized relative linear response and Responses I between m_1 and m_2, (c) Maximum Lyapunov exponent, (d) Time domain of m_0 response when $f = 260$ Hz, (e) Frequency spectra of the last 5 s of (d) (black area). The frequency spectra were obtained by FFT. The black dash line corresponds to the position of $f = 260$ Hz. The red dash line corresponds to the position of $P = 45$ μm for Response I. (For interpretation of the references to colour in this figure legend, the reader is referred to the Web version of this article.)

together as one mass, and a DOF is degenerated. Therefore, the resonance suppression in Fig. 2 (c) or 3(b) results from the transition from a 3DOF resonance region to a 2DOF non-resonance region.

To further analyze the multi-state nonlinear dynamics, we calculate the maximum Lyapunov exponent (λ_m) at each frequency, as shown in Fig. 4(c). When the collision occurs, λ_m will jump to more than 100, indicating severe chaos. We exemplify this chaos at 260 Hz using the time and spectrum analyses, as shown in Fig. 4(d) and (e). While the input frequency's amplitude remains prominent, significant responses at 201 and 435 Hz (contrasting the original linear resonances at 95 and 500 Hz) are also discernible. This means that during collisions (the chaos occurs at the same time), the total energy is redistributed towards the terminal resonances.

Although the mechanism for resonance suppression in Fig. 2(c) or 3 (b) is the transition from a resonance to a non-resonance region, the role of damping cannot be disregarded. We investigate damping's influence using $A_0 = 5$ μm as an illustrative case, as depicted in Fig. 5. In Fig. 5(a), Response I without damping (black curve) exceeds the response with damping (red curve) across all frequencies, confirming that damping attenuates the total energy in both collisional and non-collisional states. This attenuation results in a contraction of the collisional regions (the black area reduces to the red area). Similarly, reducing A_0 from 7 to 5 μm narrows the collisional region in Fig. 5(c), suggesting that the effect of damping is similar to that of a decrease in input amplitude A_0. According to the observed variation in Fig. 3, the system transforms from 3DoF to 2DOF with increasing A_0.

Consequently, the damping will decelerate the degeneration of the DOF. Notably, from the perspective of Response II, damping exhibits a contrasting effect in the second collisional region in Fig. 5(b).

A similar phenomenon occurs when A_0 decreases from 7 to 5 μm in Fig. 5(d), i.e., higher input may result in lower output. This counterintuitive result occurs because an increased input can cause the system to transition from a 3DOF to a 2DOF state within this specific frequency range.

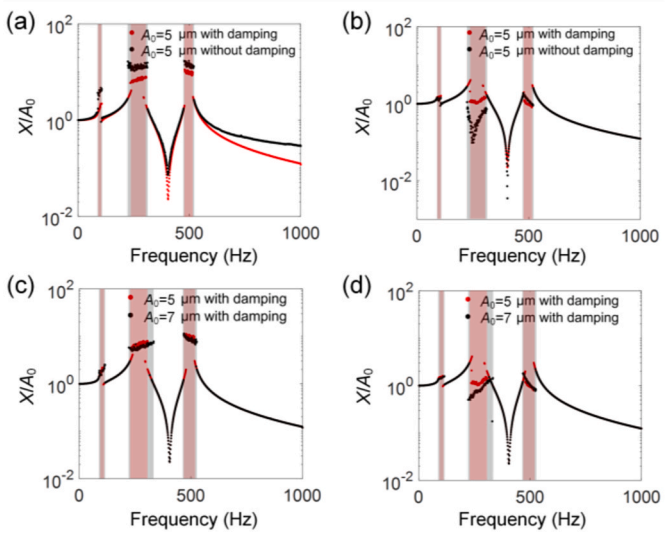

Fig. 5. Influence of damping and input amplitude A_0 for responses of m_0 in the piece-wise VI model; (a, c) Response I; (b, d) Response II; (a, b) Influence of damping; (c, d) Influence of input amplitude A_0.

3.2. Dynamics of the continuous VI model

In comparison with the piecewise VI model, approximate analytical responses for the continuous VI model can be derived using the

harmonic balance method, as illustrated in Fig. 6. These analytical solutions identify the bifurcation points—namely, the jumping points. We consider a fifth-order approximation ($n = 5$) to demonstrate the general dynamics inherent to the continuous VI model. Our focus is primarily on the applicability of the continuous VI model as an alternative to the piecewise VI model, rather than the inherent mechanisms of its nonlinear dynamics.

For weak nonlinearity at $A_0 = 1$ μm, the analytical response and Response I both show three resonances, same as that in the piece-wise VI model. As A_0 increases, the continuous VI model shows complex nonlinear dynamics, unlike the piece-wise VI model showing collisional and non-collisional dynamics. In the regime of strong nonlinearity at $A_0 = 50$ μm, the analytical response and Response I both indicate two resonances, consistent with the findings in the piecewise VI model. This similarity arises due to the large interaction force between m_1 and m_2, effectively coupling the two masses. In such a case, the analytical solution successfully predicts major Response I's behavior.

4. Similarities between the piece-wise and continuous VI models

Utilizing numerical integration methods, the difference between the piece-wise and continuous VI models, in terms of system response, can be quantified as follows:

$$\Delta = \left| \frac{\log_{10}(\text{Response I/II of equivalent model}) - \log_{10}(\text{Response I/II of vibro-impact model})}{\log_{10}(\text{Response I/II of vibro-impact model})} \right| \times 100\% \tag{6}$$

If $\Delta \leq 10$ %, it is recorded as a similar frequency point, otherwise as a dissimilar point. Consequently, within the specified frequency range, the similarity between the piece-wise and continuous VI models can be defined by a rate R:

$$R = \frac{\text{The number of similar point}}{\text{The number of total point}} \tag{7}$$

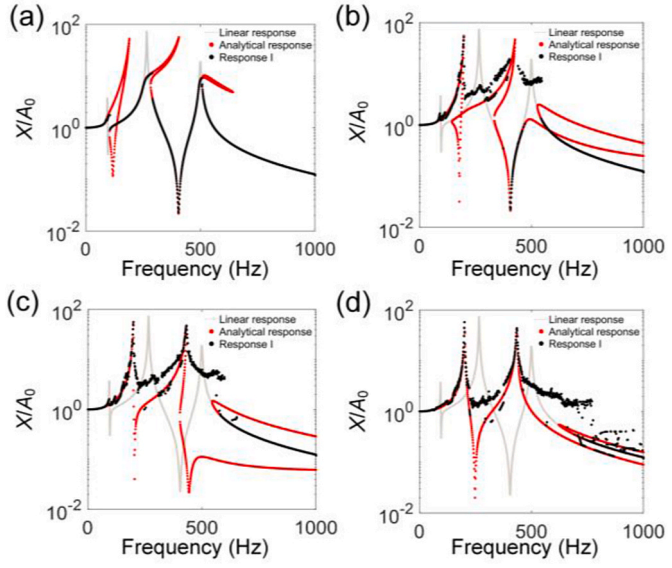

Fig. 6. Normalized response of m_0 in the continuous VI model ($n = 5$) with increasing input amplitude A_0. Four typical cases showing the variation process of Response I & II; (a) Case-1: weak nonlinearity ($A_0 = 1$ μm), (b) Case-2: moderate nonlinearity ($A_0 = 5$ μm), (c) Case-3: moderate nonlinearity ($A_0 = 10$ μm), (d) Case-4: strong nonlinearity ($A_0 = 50$ μm).

First, we investigate the similarity of a cubic VI model, $n = 3$. As shown in Fig. 7, the degree of similarity aligns with visual assessments. While increasing the amplitude A_0 from 1 to 50 μm, the similarity rate of Response I shows a decline from 83% to 42 %, whereas Response II first decreases from 83% to approximately 68% but eventually ascends to 78%.

Further investigation into the similarity rates is conducted with different nonlinear orders $k_{Nn}p^n$, or the combination $k_{N3}p^3+k_{N5}p^5+k_{N7}p^7$, as shown in Fig. 8. Although the similarity rates may fluctuate due to random overlaps (e.g. several points overlap near the resonances at 201 and 435 Hz in Fig. 7 (b) and (f)), the overarching trend of similarity rates with respect to A_0 and n is apparent. With increasing A_0, the similarity rates of Response I all decrease, while those of Response II all decrease first and increase at last. As demonstrated in section 3, both piece-wise and continuous VI models converge to a 2DOF linear system under strong nonlinearity, thereby justifying the rise in similarity rates under strong nonlinearity, as observed with Response II. However, the declining trend in similarity rates for Response I deviates from this expectation, prompting further exploration into the chaotic dynamics in subsequent analyses.

As n increases, both Responses I and II generally exhibit higher similarity rates. The case with combined nonlinear terms $k_{N3}p^3+k_{N5}p^5+k_{N7}p^7$ shows a lower similarity rate than that with $k_{N7}p^7$, indicating that the similarity rate of the polynomial combination is dominated by the maximum n. This aligns with the fitting result shown in Fig. 1(c): fitting curves approximate the actual curve more closely with increasing n, and the polynomial fitting curve lies between the curves for $n = 5$ and 7. In addition to response similarity, we compare λ_m of the piece-wise and continuous VI models in Fig. 10(d).

Similarly, an increase in n leads to the λ_m of the continuous model approaching that of the piecewise model, indicating that a larger n value enhances the likeness between the models. Thus, we calculate the similarity rate of Responses I and II for substantially large n values ($n = 29$, 35 and 47), as shown in Fig. 9. The overall similarity rates all increase to more than 80%. However, both analytical and numerical calculations become more time-consuming with larger n. Consequently, a balance must be struck between the computation time, accuracy, and the chosen value of n when substituting the piecewise VI model with the continuous model. Furthermore, moderate nonlinearity is occasionally overlooked, such as in band structure calculations [41], rendering $n = 5$ or 7 as satisfactory equivalents. Apart from the similarity of the response, we also investigate the similarity of the chaotic dynamics in piece-wise and continuous VI models, as shown in Fig. 10. Here we take the order $n = 5$ to illustrate the chaotic dynamics of the continuous VI model.

For weak nonlinearity at $A_0 = 1$ μm, both λ_{m_pie} and λ_{m_con} approximate zero at all frequencies, as shown in Fig. 10(a) and (b). With increasing A_0, the frequencies where λ_{m_pie}, $\lambda_{m\_con} > 0$ become more prevalent, indicating that the collisional region replaces the non-collisional region in the piece-wise VI model. This transition reflects the evolution of multi-state dynamics from a chaotic perspective. Concurrently, when a collision occurs (λ_{m_pie}, $\lambda_{m\_con} > 0$), both λ_{m_pie} and λ_{m_con} become larger, signaling increased chaos. To better show this specific variation, we adopt a typical time signal and frequency spectrum at 260 Hz as shown in Fig. 10(e) and (f). With increasing A_0 (more severe chaos), the original resonance (266 Hz) transfers to the terminal resonances (201 and 435 Hz) as observed in the frequency spectra, which move further from 260 Hz. Concurrently, the transmission decreases. Thus, as a whole, the larger the exponents λ_{m_pie} and λ_{m_con}, the lower the vibration transmission. Under strong nonlinearity at $A_0 = 50$ μm, λ_{m_pie} and λ_{m_con} both have the same two resonances at 201 and 435 Hz, aligning with the response. Overall, the trends of λ_{m_pie} and λ_{m_con} are similar, signifying that the piece-wise and continuous VI models

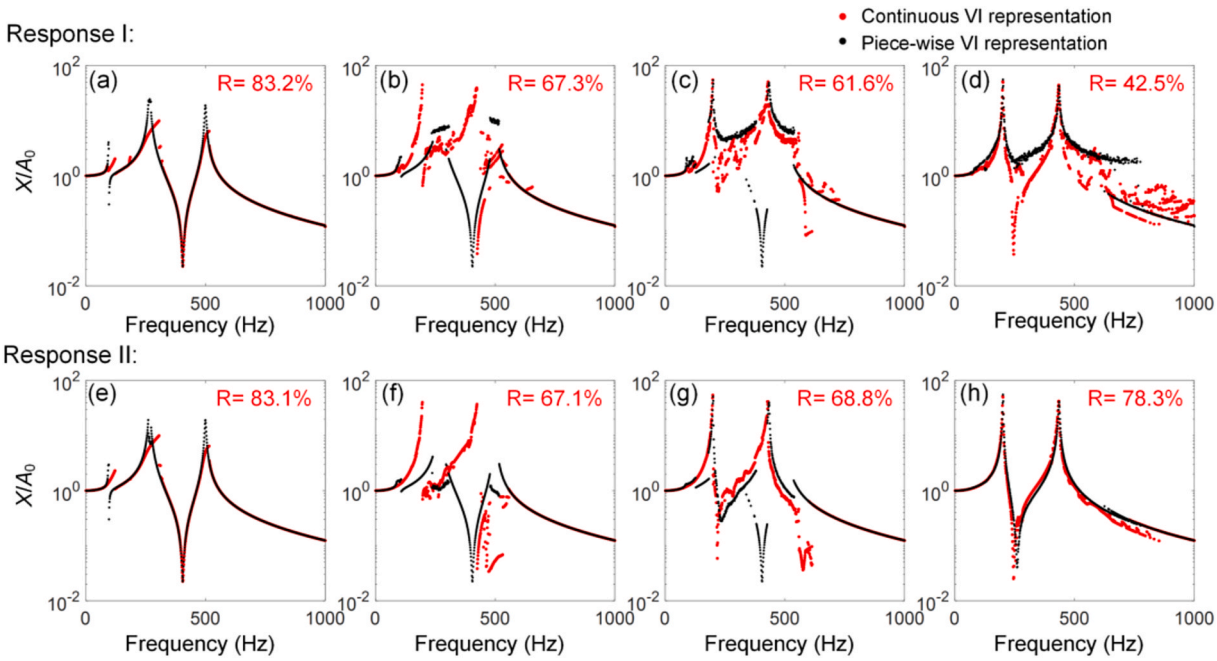

Fig. 7. The variation of similarity rate between continuous VI model ($n = 3$) and piece-wise VI model with increasing input amplitude A_0. (a–d) Response I, (e–f) Response II, (a, e) Case-1: weak nonlinearity ($A_0 = 1$ μm), (b, f) Case-2: moderate nonlinearity ($A_0 = 5$ μm), (c, g) Case-3: moderate nonlinearity ($A_0 = 10$ μm), (d, h) Case-4: strong nonlinearity ($A_0 = 50$ μm).

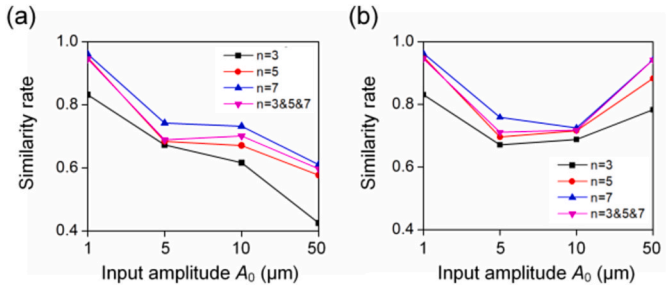

Fig. 8. The variation of similarity rate between different continuous VI models and piece-wise VI model with increasing input amplitude A_0. (a) Response I, (b) Response II. Continuous VI models (n = 3&5&7) means that a continuous function $k_{N3}p^3 + k_{N5}p^5 + k_{N7}p^7$ is used to replace the symmetrical piece-wise function.

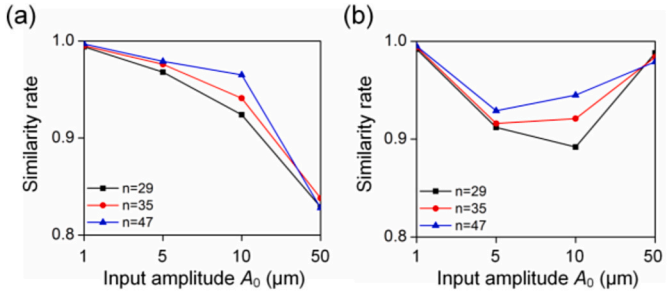

Fig. 9. The variation of similarity rate between extreme continuous VI models (n is extreme large) and piece-wise VI model with increasing input amplitude A_0. (a) Response I, (b) Response II.

share similar chaotic dynamics.

Despite the analogous trend of the chaotic dynamics, λ_{m_pie} and λ_{m_con} differ between the piece-wise and continuous VI models. We calculate the values of $\lambda_{m\_pie} - \lambda_{m\_con}$ to illuminate the specific differences as shown in Fig. 10(c) $\lambda_{m\_pie} - \lambda_{m\_con} \neq 0$ indicates differing strengths of chaos, leading to varied transmissions in the time domain between the piece-wise and continuous VI models. As A_0 increases, there are more frequencies with $\lambda_{m\_pie} - \lambda_{m\_con} \neq 0$, indicating that the similarity of transmission diminishes, i.e., the similarity rate of Response I decreases.

Upon examining the nonlinear dynamics and similarity attributes between the piece-wise and continuous VI models, we observe that Response II maintains a high similarity rate for both weak ($A_0 \leq 1$ μm) and strong nonlinearity cases ($A_0 \geq 50$ μm). Conversely, it exhibits a low similarity rate under moderate nonlinearity ($A_0 = 1$–50 μm). As indicated in Fig. 5, decreasing damping emerges as an effective strategy to abbreviate this transition. However, damping can also dampen Response I (the overall energy) to ensure system safety. Consequently, the specific damping value must be determined according to the actual requirements and conditions. Additionally, reducing the clearance δ between m_1 and each stop can be effective.

Fig. 11 shows that when the input amplitudes are equal to the clearance δ, Responses I and II both express two resonances regardless of clearance δ, consistent with the results presented in Fig. 3(d). Nonetheless, δ cannot be reduced infinitely due to limitations imposed by manufacturing precision in reality. Therefore, minimizing the clearance δ to a practical and reasonable value is an effective way to narrow the gap between weak and strong nonlinearity.

5. Experimental validation

An experiment was meticulously designed and carried out to demonstrate the multi-state and chaotic dynamics of the system, as observed in the piece-wise VI model. As shown in Fig. 12(b), the specimen is identical to the unit cell proposed by Fang et al. [12], with the same set of parameters and structure as those of Fig. 1(a). Each spring is affixed to the corresponding masses and the shaker using cyanoacrylate adhesive. A symmetrical clearance, $\delta = 45 \pm 15$μm, is established between the sphere m_1 and the cylinder wall m_2 at rest. As shown in Fig. 12 (a), a signal generator (Tektronix, AFG1022X) supplies the input signal coded by a computer, to a power amplifier (Brüel&kjær, Type 2706). The power amplifier boosts the input signal by 10 dB and drives the shaker (Brüel&kjær, Type 4809). A Doppler Laser Vibrometer (Polytec,

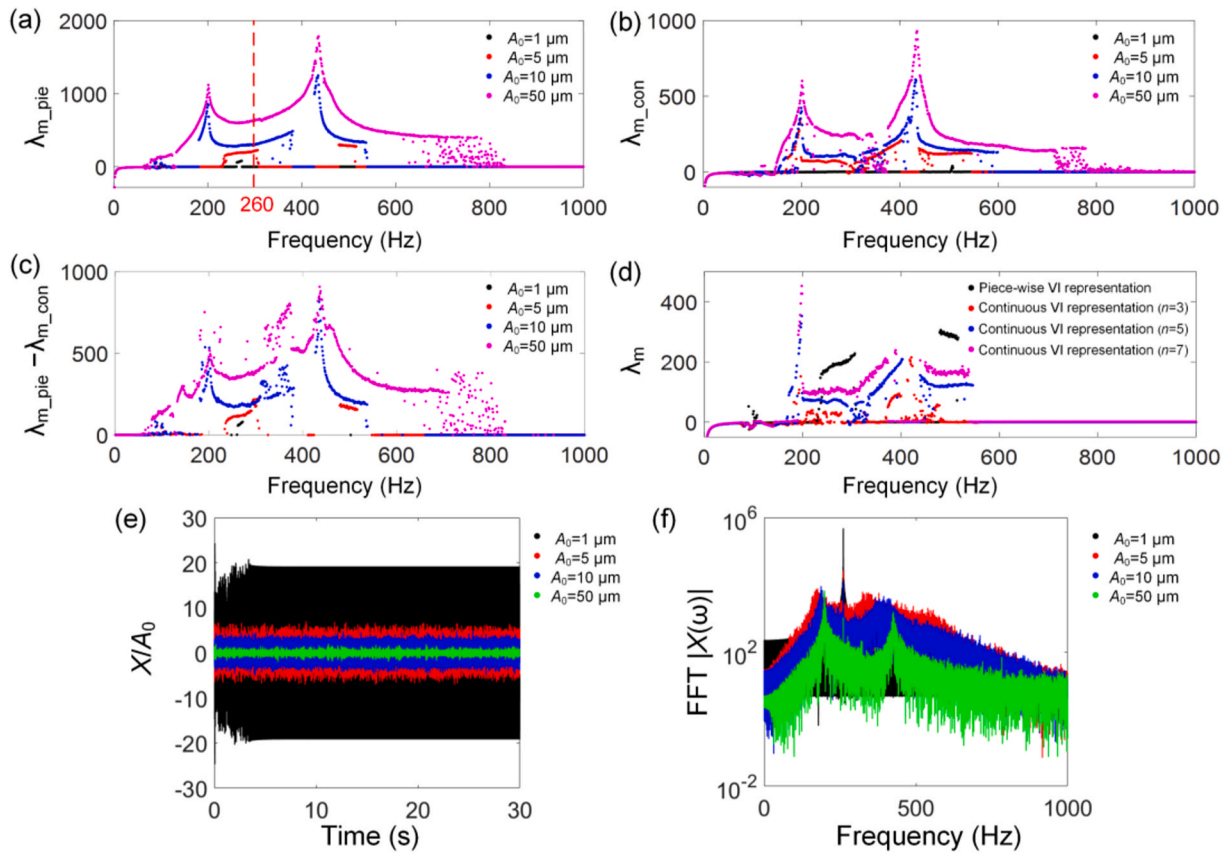

Fig. 10. Maximum Lyapunov exponents λ_m. (a) λ_{m_pie} of VI piece-wise model with increasing A_0, (b) λ_{m_con} of continuous VI model ($n = 5$) with increasing A_0, (c) $\lambda_{m\_pie}-\lambda_{m\_con}$ with increasing A_0, (d) λ_m of different continuous VI models and piece-wise VI model with moderate nonlinearity ($A_0 = 5$ μm), (e) Time domain at 260 Hz of the piece-wise VI model in (a) with increasing A_0 (f) Frequency spectra for the last 5 s of (e).

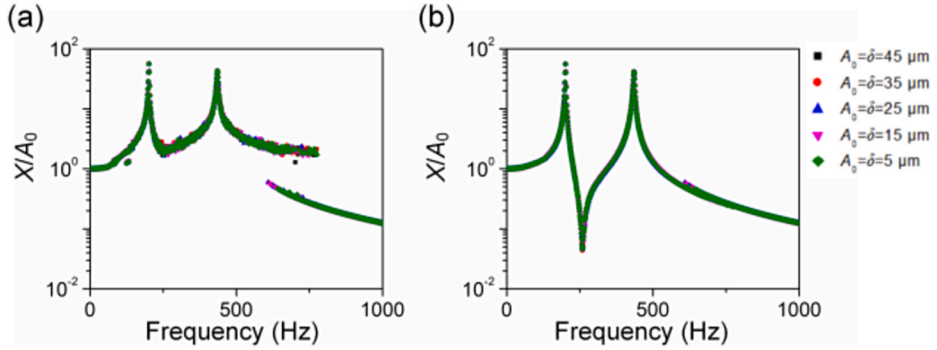

Fig. 11. Normalized responses of m_0 in the piece-wise VI model with different clearance δ when input amplitude $A_0 = \delta$. (a) Response I, (b) Response II.

PSV-500) records the velocity of the primary mass m_0 and transmits the data to a computer for further processing. Utilizing white-noise signals at different voltages V_0, we take $V_0 = 0.05$, 1.5, 10 V to represent the weak, moderate, and strong nonlinear states, with results shown in Fig. 13.

As shown in Fig. 13(a), under a low input $V_0 = 0.05$ V, both the measured response curve and calculated Response I show three resonances at 95, 266 and 500 Hz. In line with numerical predictions, the measured transmission at these three resonances is reduced when increasing V_0. However, distinguishing the multi-state dynamics (collisional and non-collisional regions) is challenging due to the inherent randomness introduced by the white noise input. Instead, we utilize a sine-sweep signal to illustrate the multi-state dynamics, as shown in Fig. 13(d). During the sweep test, the excitation frequency gradually increases from 150 to 350 Hz within 200 s. In the beginning, the time-domain envelope of the measured signal steadily rises, showing the dynamics in the non-collisional region. Roughly from 90 to 140 s (the grey area of about 240–290 Hz), the envelope becomes unstable because the collision between m_1 and m_2 occurs. Subsequently, the response envelope smoothly decreases, signaling a return to non-collisional region dynamics. Both time- and frequency-domain results corroborate the existence of multi-state dynamics in the piece-wise VI model. Under strong nonlinearity with $V_0 = 10$ V, the experimental response and Response I of the simulation both show two terminal resonances at 201 and 435 Hz as shown in Fig. 13(c). A slight discrepancy in the peak frequencies at these resonances is likely due to damping effects and other uncertain factors.

Furthermore, we analyze the time signal and frequency spectrum

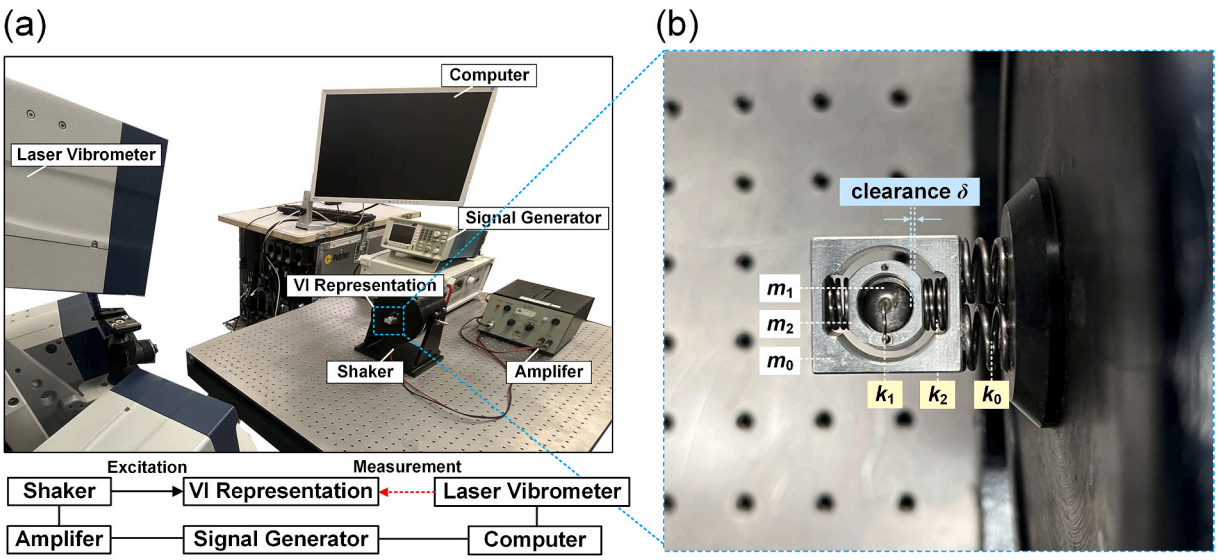

Fig. 12. Experimental setup. (a) System for measuring the response of the specimen, (b) Experimental specimen of the piece-wise VI model.

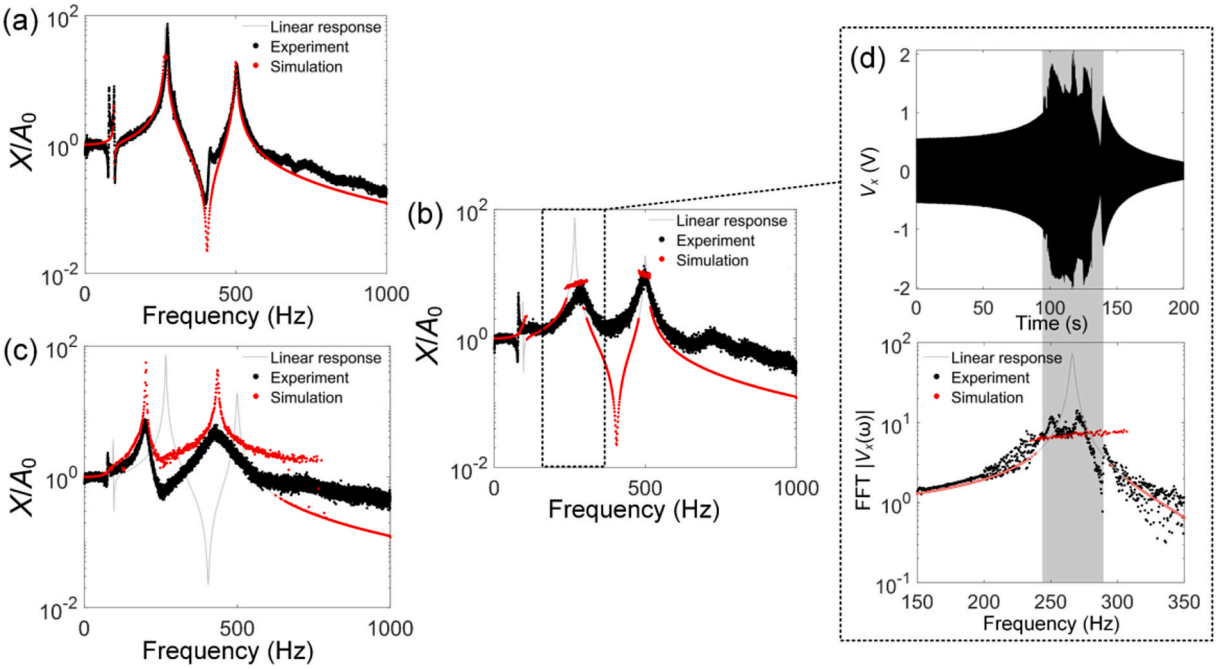

Fig. 13. Normalized response of m_0 in the experiment of the piece-wise VI model with increasing input voltage A_0. Herein, we take four typical cases to show the variation process of Response I of the simulation and experimental response. (a) Case-1: weak nonlinearity ($V_0 = 0.05$ V for the experiment, $A_0 = 1$ μm for the simulation), (b) Case-2: moderate nonlinearity ($V_0 = 1.5$ V, $A_0 = 5$ μm), (c) Case-4: strong nonlinearity ($V_0 = 10$ V, $A_0 = 50$ μm). (d) Time and frequency spectrum of the voltage response V_x by the excitation of the sweep signal. The voltage and frequency range of the sweep signal correspond to those of (b).

around 260 Hz to clarify the experimental occurrence of chaos, as illustrated in Fig. 14. As V_0 increases, the transmission in the time domain declines. Concurrently, two additional resonances emerge and approach the terminal resonances (201 and 435 Hz), with the spectra indicating escalating chaos. These observations are congruent with those from Fig. 10, thereby affirming the experimental results are in substantial agreement with numerical predictions, validating the multi-state and chaotic dynamics anticipated by the piece-wise VI model.

6. Conclusions

In this paper, a typical 3DoF VI system is rigorously examined both numerically and experimentally to elucidate its multi-state chaotic dynamics. We propose a criterion for equating the piecewise VI system with a continuous VI system, which serves to streamline the modeling process and potentially accelerate the calculation and simulation of the high-dimensional VI system. The similarity of response and chaotic dynamics between the piecewise and continuous nonlinear VI systems is investigated to confirm the validity and the reliability of this equivalence. With increasing nonlinearity, the 3DOF VI system degenerates to a 2DOF system due to the collisional and non-collisional states between the two oscillators. This transition results in discontinuous multi-state transmission curves and simultaneous suppression of system resonances.

To accelerate calculation in high-dimensional VI systems, one can equate a piece-wise VI system to a continuous nonlinear system incorporating nonlinear terms, $k_{Nn}p^n$, or their combination,

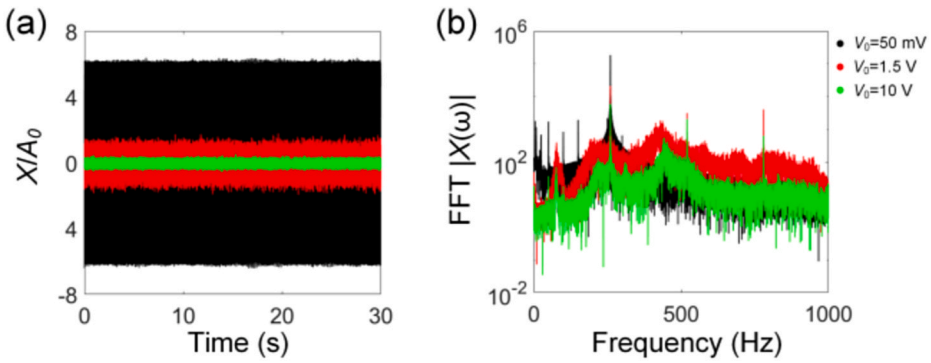

Fig. 14. Experimental responses at 260 Hz of the piece-wise VI model with increasing V_0 (a) Time domain (b) Frequency spectra for the last 5 s of (a).

$k_{N3}p^3+k_{N5}p^5+k_{N7}p^7$. The focus here is on the criteria for this equivalence. Given that a small dynamic load between m_1 and m_2 can induce only minor contact deformation at the boundary, we take the contact force at a contact deformation of 1 μm to derive the nonlinear or combined terms. It is found that employing higher nonlinear order functions, $k_{Nn}p^n$ yields a response of the VI model that is more closely aligned with that of the continuous VI model, albeit at the expense of increased computational time. The similarity rate of the polynomial combination is dictated by the highest order n. Although both the piecewise and continuous models exhibit comparable chaotic dynamics, the piecewise VI model exhibits stronger chaos, leading to a reduced similarity in the time-domain response curves, namely, Response I. Meanwhile, reducing damping and the collision gap enhances the similarity across a broad spectrum of nonlinearities.

This work advances our comprehension of the multi-state chaotic dynamics in VI systems and delivers a framework for the accurate and efficient modeling of high-dimensional, strongly nonlinear systems in future investigations.

CRediT authorship contribution statement

Chen Gong: Writing – review & editing, Writing – original draft, Validation, Methodology, Investigation, Formal analysis, Data curation. **Xin Fang:** Writing – review & editing, Supervision, Resources, Project administration, Funding acquisition, Formal analysis, Conceptualization. **Li Cheng:** Writing – review & editing, Supervision, Resources, Project administration, Funding acquisition, Formal analysis.

Declaration of competing interest

The authors declare that they have no known competing financial interests or personal relationships that could have appeared to influence the work reported in this paper.

Data availability

Data will be made available on request.

Acknowledgements

This research was funded by the Research Grant Council of the Hong Kong SAR through a GRF project. Xin Fang is supported by the National Natural Science Foundation of China (Projects No. 52241103 and No. 52322505) and the Hong Kong Scholars Program.

References

[1] M.A. Al-Shudeifat, N. Wierschem, D.D. Quinn, A.F. Vakakis, L.A. Bergman, B. F. Spencer Jr., Numerical and experimental investigation of a highly effective single-sided vibro-impact non-linear energy sink for shock mitigation, Int. J. Non Lin. Mech. 52 (2013) 96–109, https://doi.org/10.1016/j.ijnonlinmec.2013.02.004.

[2] P. Balaji, K. Karthik SelvaKumar, Applications of nonlinearity in passive vibration control: a review, J. Vib. Eng. Technol. 9 (2021) 183–213, https://doi.org/10.1007/s42417-020-00216-3.

[3] T. Emerson, J. Manimala, Passive-adaptive mechanical wave manipulation using nonlinear metamaterial plates, Acta Mech. 231 (2020) 4665–4681, https://doi.org/10.1007/s00707-020-02782-9.

[4] T. Yang, S. Zhou, S. Fang, W. Qin, D.J. Inman, Nonlinear vibration energy harvesting and vibration suppression technologies: designs, analysis, and applications, Appl. Phys. Rev. 8 (3) (2021) 031317, https://doi.org/10.1063/5.0051432.

[5] H. Ding, L.-Q. Chen, Designs, analysis, and applications of nonlinear energy sinks, Nonlinear Dynam. 100 (4) (2020) 3061–3107, https://doi.org/10.1007/s11071-020-05724-1.

[6] Z. Lu, Z. Wang, Y. Zhou, X. Lu, Nonlinear dissipative devices in structural vibration control: a review, J. Sound Vib. 423 (2018) 18–49, https://doi.org/10.1016/j.jsv.2018.02.052.

[7] A.S. Saeed, R. Abdul Nasar, M.A. Al-Shudeifat, A review on nonlinear energy sinks: designs, analysis and applications of impact and rotary types, Nonlinear Dynam. (2022) 1–37, https://doi.org/10.1007/s11071-022-08094-y.

[8] S. Li, J. Li, H. Zhu, S.-K. Lai, Dynamical analysis and numerical verification of a non-smooth nonlinear energy sink, Int. J. Non Lin. Mech. 151 (2023) 104381, https://doi.org/10.1016/j.ijnonlinmec.2023.104381.

[9] G.U. Patil, K.H. Matlack, Review of exploiting nonlinearity in phononic materials to enable nonlinear wave responses, Acta Mech. 233 (1) (2022) 1–46, https://doi.org/10.1007/s00707-021-03089-z.

[10] M. Yu, X. Fang, D. Yu, Combinational design of linear and nonlinear elastic metamaterials, Int. J. Mech. Sci. 199 (2021) 106422, https://doi.org/10.1016/j.ijmecsci.2021.106422.

[11] X. Fang, P. Sheng, J. Wen, W. Chen, L. Cheng, A nonlinear metamaterial plate for suppressing vibration and sound radiation, Int. J. Mech. Sci. 228 (2022) 107473, https://doi.org/10.1016/j.ijmecsci.2022.107473.

[12] X. Fang, J. Wen, H. Benisty, D. Yu, Ultrabroad acoustical limiting in nonlinear metamaterials due to adaptive-broadening band-gap effect, Phys. Rev. B 101 (10) (2020) 104304, https://doi.org/10.1103/PhysRevB.101.104304.

[13] D.M. McFarland, L.A. Bergman, A.F. Vakakis, Experimental study of non-linear energy pumping occurring at a single fast frequency, Int. J. Non Lin. Mech. 40 (6) (2005) 891–899, https://doi.org/10.1016/j.ijnonlinmec.2022.104285.

[14] Y.S. Lee, G. Kerschen, A.F. Vakakis, P. Panagopoulos, L. Bergman, D.M. McFarland, Complicated dynamics of a linear oscillator with a light, essentially nonlinear attachment, Physica D 204 (1–2) (2005) 41–69, https://doi.org/10.1016/j.physd.2005.03.014.

[15] D.M. McFarland, L.A. Bergman, A.F. Vakakis, Experimental study of non-linear energy pumping occurring at a single fast frequency, Int. J. Non Lin. Mech. 40 (6) (2005) 891–899, https://doi.org/10.1016/j.ijnonlinmec.2004.11.001.

[16] M.A. Al-Shudeifat, N.E. Wierschem, L.A. Bergman, A.F. Vakakis, Numerical and experimental investigations of a rotating nonlinear energy sink, Meccanica 52 (2017) 763–779, https://doi.org/10.1007/s11012-016-0422-2.

[17] G. Sigalov, O. Gendelman, M. Al-Shudeifat, L. Manevitch, A. Vakakis, L. Bergman, Resonance captures and targeted energy transfers in an inertially-coupled rotational nonlinear energy sink, Nonlinear Dynam. 69 (2012) 1693–1704, https://doi.org/10.1007/s11071-012-0379-1.

[18] G. Sigalov, O. Gendelman, M. Al-Shudeifat, L. Manevitch, A. Vakakis, L. Bergman, Alternation of regular and chaotic dynamics in a simple two-degree-of-freedom system with nonlinear inertial coupling, Chaos 22 (1) (2012) 013118, https://doi.org/10.1063/1.3683480.

[19] Y. Cao, H. Yao, Q. Li, P. Yang, B. Wen, Vibration mitigation and dynamics of a rotor-blade system with an attached nonlinear energy sink, Int. J. Non Lin. Mech. 127 (2020) 103614, https://doi.org/10.1016/j.ijnonlinmec.2020.103614.

[20] X. Lu, Z. Liu, Z. Lu, Optimization design and experimental verification of track nonlinear energy sink for vibration control under seismic excitation, Struct. Control Health Monit. 24 (12) (2017) e2033, https://doi.org/10.1002/stc.2033.

[21] J. Wang, N. Wierschem, B.F. Spencer Jr., X. Lu, Experimental study of track nonlinear energy sinks for dynamic response reduction, Eng. Struct. 94 (2015) 9–15, https://doi.org/10.1016/j.engstruct.2015.03.007.

[22] J. Wang, N.E. Wierschem, B.F. Spencer Jr., X. Lu, Track nonlinear energy sink for rapid response reduction in building structures, J. Eng. Mech. 141 (1) (2015) 04014104, https://doi.org/10.1061/(ASCE)EM.1943-7889.0000824.
[23] E. Gourc, G. Michon, S. Seguy, A. Berlioz, Targeted energy transfer under harmonic forcing with a vibro-impact nonlinear energy sink: analytical and experimental developments, J. Sound Vib. 137 (3) (2015), https://doi.org/10.1115/1.4029285.
[24] I. Karayannis, A. Vakakis, F. Georgiades, Vibro-impact attachments as shock absorbers, Proc. Inst. Mech. Eng. C J. Mech. Eng. Sci. 222 (10) (2008) 1899–1908, https://doi.org/10.1243/09544062JMES864.
[25] Z. Wu, M. Paredes, S. Seguy, Targeted energy transfer in a vibro-impact cubic NES: description of regimes and optimal design, J. Sound Vib. 545 (2023) 117425, https://doi.org/10.1016/j.jsv.2022.117425.
[26] S. Li, H. Wu, J. Chen, Global dynamics and performance of vibration reduction for a new vibro-impact bistable nonlinear energy sink, Int. J. Non Lin. Mech. 139 (2022) 103891, https://doi.org/10.1016/j.ijnonlinmec.2021.103891.
[27] F. Georgiadis, A.F. Vakakis, D.M. McFarland, L. Bergman, Shock isolation through passive energy pumping caused by nonsmooth nonlinearities, Int. J. Bifurcat Chaos. 15 (6) (2005) 1989–2001, https://doi.org/10.1142/S0218127405013101.
[28] F. Nucera, F.L. Iacono, D.M. McFarland, L. Bergman, A. Vakakis, Application of broadband nonlinear targeted energy transfers for seismic mitigation of a shear frame: experimental results, J. Sound Vib. 313 (1–2) (2008) 57–76, https://doi.org/10.1016/j.jsv.2007.11.018.
[29] F. Nucera, D.M. McFarland, L. Bergman, A. Vakakis, Application of broadband nonlinear targeted energy transfers for seismic mitigation of a shear frame: computational results, J. Sound Vib. 329 (15) (2010) 2973–2994, https://doi.org/10.1016/j.jsv.2010.01.020.
[30] F. Nucera, A.F. Vakakis, D.M. McFarland, L. Bergman, G. Kerschen, Targeted energy transfers in vibro-impact oscillators for seismic mitigation, Nonlinear Dynam. 50 (2007) 651–677, https://doi.org/10.1007/s11071-006-9189-7.
[31] Y.S. Lee, F. Nucera, A.F. Vakakis, D.M. McFarland, L.A. Bergman, Periodic orbits, damped transitions and targeted energy transfers in oscillators with vibro-impact attachments, Physica D 238 (18) (2009) 1868–1896, https://doi.org/10.1016/j.physd.2009.06.013.
[32] H. Tao, J. Gibert, Periodic orbits of a conservative 2-DOF vibro-impact system by piecewise continuation: bifurcations and fractals, Nonlinear Dynam. 95 (2019) 2963–2993, https://doi.org/10.1007/s11071-018-04734-4.
[33] X. Fang, J. Wen, B. Bonello, J. Yin, D. Yu, Ultra-low and ultra-broad-band nonlinear acoustic metamaterials, Nat. Commun. 8 (1) (2017) 1288, https://doi.org/10.1038/s41467-017-00671-9.
[34] X. Fang, J. Wen, D. Yu, J. Yin, Bridging-coupling band gaps in nonlinear acoustic metamaterials, Phys. Rev. Appl. 10 (5) (2018) 054049, https://doi.org/10.1103/PhysRevApplied.10.054049.
[35] X. Fang, J. Wen, L. Cheng, B. Li, Bidirectional elastic diode with frequency-preserved nonreciprocity, Phys. Rev. Appl. 15 (5) (2021) 054022, https://doi.org/10.1103/PhysRevApplied.15.054022.
[36] Heinrich Hertz, Über die Berührung fester elastischer Körper, J. für die Reine Angewandte Math. (Crelle's J.) 92 (1881) 156.
[37] G. Theocharis, N. Boechler, C. Daraio, Acoustic Metamaterials and Phononic Crystals, vol. 173, Springer Science & Business Media, 2013, pp. 217–251.
[38] J. Lydon, G. Theocharis, C. Daraio, Nonlinear resonances and energy transfer in finite granular chains, Phys. Rev. E 91 (2) (2015) 023208, https://doi.org/10.1103/PhysRevE.91.023208.
[39] N. Boechler, G. Theocharis, S. Job, P.G. Kevrekidis, Mason A. Porter, C. Daraio, Discrete breathers in one-dimensional diatomic granular crystals, Phys. Rev. Lett. 104 (2010) 244302, https://doi.org/10.1103/PhysRevLett.104.244302.
[40] E. Dintwa, E. Tijskens, H. Ramon, On the accuracy of the Hertz model to describe the normal contact of soft elastic spheres, Granul. Matter 10 (2008) 209–221, https://doi.org/10.1007/s10035-007-0078-7.
[41] C. Gong, X. Fang, L. Cheng, Band degeneration and evolution in nonlinear triatomic metamaterials, Nonlinear Dynam. 111 (1) (2023) 97–112, https://doi.org/10.1007/s11071-022-07860-2.

Chen Gong
Department of Mechanical Engineering, Hong Kong Polytechnic University, Hong Kong

Xin Fang*
Laboratory of Science and Technology on Integrated Logistics Support, College of Intelligent Science, National University of Defense Technology, Changsha, Hunan, 410073, China

Li Cheng**
Department of Mechanical Engineering, Hong Kong Polytechnic University, Hong Kong

* Corresponding author.

** Corresponding author.
E-mail address: xinfangdr@sina.com (X. Fang).
E-mail address: li.cheng@polyu.edu.hk (L. Cheng).